PROCEEDINGS, 45th Workshop on Geothermal Reservoir Engineering
Stanford University, Stanford, California, February 10-12, 2020
SGP-TR-216

Application of an Embedded Fracture and Borehole Modeling Approach to the Understanding of EGS Collab Experiment 1

Mark D. White[1], Pengcheng Fu[2], and EGS Collab Team[3]

[1]Energy and Environment Directorate, Pacific Northwest National Laboratory, Richland, WA 99352, USA

[2]Atmospheric, Earth and Energy Division, Lawrence Livermore National Laboratory, Livermore, CA 94550, USA

E-mail address, mark.white@pnnl.gov

Keywords: Numerical Simulation, Embedded Fractures and Boreholes, EGS Collab, Meso-Scale EGS Experiment, Sanford Underground Research Facility, Thermal Recovery, Conservative and Sorbing Tracers

ABSTRACT

EGS Collab is a series of meso-scale experiments and associated numerical simulation activities being funded by the United States Department of Energy, Geothermal Technologies Office (GTO) to investigate enhanced geothermal system processes under in-situ stress and slightly elevated temperature conditions. This project is designed to provide scientists and engineers with immediate access to impermeable rock at scales larger than possible in the laboratory, but generally smaller than those for commercial production. Immediate access to rock is provided via the existing drifts of the former Homestake Gold Mine, now operated as the Sanford Underground Research Facility in Lead, South Dakota. The objectives of the EGS Collab project are to develop well controlled fracture networks between injector and producer boreholes using normal and shear stimulation for permeability enhancement. The first experimental site was located off the West Access drift on the 4850 Level (4850 feet below ground surface) in phyllite of the Precambrian Poorman formation, and involved the creation of a fracture network comprising a combination of hydraulic and natural fractures. A second experimental site is now being considered near the battery alcove on the 4100 Level in amphibolite and rhyolite of the Yates Unit. Data generated during these experiments will be compared against predictions of a suite of computer codes specifically designed to solve problems involving coupled thermal, hydrological, geomechanical, and geochemical processes. Comparisons between experimental and numerical simulation results will provide code developers with direction for improvements and verification of process models, build confidence in the suite of available numerical tools, and ultimately identify critical future development needs for the geothermal modeling community. Moreover, conducting thorough comparisons of models, modelling approaches, measurement approaches and measured data, via the EGS Collab project, will serve to identify techniques that are most likely to succeed at the Frontier Observatory for Research in Geothermal Energy (FORGE), the GTO's flagship EGS research effort. Experiment 1 has comprised a series of successful tests, including a long-term chilled-water circulation test, but the testbed has two atypical EGS elements. Active ventilation in the adjacent drift over a 50-year period cooled the testbed rock mass and hydraulic fracturing intersected monitoring boreholes making them conduits for fluid flow. Numerical simulations executed in support of the design of the EGS Collab Experiment 1, computed a radial temperature distribution and stress gradient orthogonal to the drift axis, resulting in the forecast of an oblong hydraulic fracture geometry, extended in the direction of the drift from the stimulation borehole. This paper describes the numerical simulation of long-term chilled-water circulation test with an embedded fracture and borehole modeling approach. The principal objective of the simulation work is show agreement between experimental observations in terms of production fluid temperatures, monitoring borehole temperatures, injection and production pressures, and tracer recoveries using a single conceptual model for the fracture network, using characterization and monitoring data generally available for EGS. A secondary objective is to improve the numerical simulation result comparisons with additional data available from the broader monitoring equipment within the testbed versus deeper, hotter, and more remote EGS. One complicating factor for comparisons between the numerical simulation results and experimental observations, is the Joule-Thomson heating associated with large pressure drops across the fracture network.

1. INTRODUCTION

Since early 2017, the United States Department of Energy (DOE), Geothermal Technologies Office (GTO) has been sponsoring a meso-scale experiment and numerical validation study to serve as a research and development path between laboratory-scale stimulation and rock mechanics studies and the large field scale of the future Frontier Observatory for Research in Geothermal Energy (FORGE) investigations (U.S. Department of Energy, 2017). This project, the Stimulation Investigations for Geothermal Modeling Analysis and Validation, termed EGS Collab, is being led by the Lawrence Berkeley National Laboratory (LBNL), but is a highly collaborative venture involving seven U.S. National Laboratories, universities, and private industry (Dobson et al., 2017; Kneafsey et al., 2018; Kneafsey et al., 2019). Principal objectives of the EGS Collab project are to develop experimental testbeds with normal- and shear-opening fracture networks between hydraulically connected boreholes under representative EGS stress conditions, but low temperature conditions, and then to compare numerical simulation forecasts against the experimental observations. Numerical simulations over the course of the project have been applied to guide experiment design, forecast fracture network initiation, development and extension, and validate the use of conservative and partitioning tracer recovery as an analog for thermal recovery and reservoir performance.

Code verification is a critical element in the advancement of numerical simulators for enhanced geothermal systems (EGS). DOE has supported the development and verification of numerical simulators throughout the history of EGS research, starting with the Finite Element Heat and Mass (FEHM), HDR Heat, and GEOCRACK models (Duchane and Winchester, 1992; Zyvoloski, 2007), used to

estimate the potential thermal lifetime of the Phase II Reservoir at Fenton Hill. More recently GTO sponsored a multiple-year code comparison study that considered nine benchmark problems and two challenge problems (White, Fu, McClure, et al., 2018; White et al., 2016a, b). The benchmark problems were structured to test the ability of the collection of numerical simulators to solve various combinations of coupled thermal, hydrologic, geomechanical, and geochemical processes. This class of problems was strictly defined in terms of properties, driving forces, initial conditions, and boundary conditions.

Hill Hot Dry Rock (HDR) project involved the stimulation, completion, and circulation testing in two separate reservoirs, distinguished by depth and flow complexity. Both challenge problems have specific questions to be answered via numerical simulation in three topical areas: 1) reservoir creation/stimulation, 2) reactive and passive transport, and 3) thermal recovery. Whereas the benchmark class of problems were designed to test capabilities for modeling coupled processes under strictly specified conditions, the stated objective for the challenge class of problems was to demonstrate what new understanding of the Fenton Hill experiments could be realized via the application of modern numerical simulation tools by recognized expert practitioners. Critical observations and data from the Fenton Hill experiments were varied and scattered among a number of individual experiments, and numerical simulation solutions were sought that satisfied as many observations at possible. Achieving agreement in multiple experimental observations from Fenton Hill often required participants to critically think about stimulation mechanisms involving natural and hydraulic fractures and re-evaluate their conceptual models and numerical solution approaches. This process has yielded new insights to Fenton Hill reservoirs and direction for future EGS research.

The EGS Collab project is a recognition of the importance of validating numerical simulation tools for EGS, and the meso-scale of the experiments and accessibility of the generated fracture networks under in-situ stress conditions and crystalline rock formations, and provides a unique opportunity for the validation of THMC modeling approaches. The EGS Collab project comprises three major experiments, occurring over the course of the three-year project duration. Each major experiment is composed of a series of smaller stimulation and circulation experiments. Prior to each experiment site characterization was conducted and numerical simulations were executed to guide the experimental design and monitoring systems. After each experiment, numerical simulations will be executed, and results compared against the collected data. The diversity of the EGS Collab teams brings a spectrum of numerical approaches for modeling THMC processes for EGS (White, Fu, Ghassemi, et al., 2018; White, Fu, Huang, et al., 2018; White et al., 2019). The post experimental period will allow for comparison of these numerical approaches and an assessment of code limitations, need improvements, or alterations to conceptual models.

EGS Collab Experiment 1 is being conducted with a volume of predominately phyllite rock on the western side of the 4850 Level West Access Drift (drift) within Sanford Underground Research Facility (SURF) near the kISMET site (Oldenburg et al., 2016). This experiment involves two stages: 1) stimulation - the creation of a hydraulic fracture from a sub-horizontal borehole drilled nominally in the direction of the principal minimum horizontal stress (i.e., S_{hmin}); and 2) circulation – the circulation of fluids between an injection well and one or more production wells intersecting the created fracture. At this writing, a series of eight boreholes have been drilled from the drift: 1) injection [E1-I], 2) production [E1-P], 3) two fracture orthogonal monitoring [E1-OT, E1-OB], 4) two deep fracture parallel monitoring [E1-PDT, E1-PDB], and 5) two shallow fracture parallel monitoring [E1-PST, E1-PSB]. The injection and production boreholes were drilled in the anticipated direction of S_{hmin}, (i.e., with a 356° trend and 12° plunge). The two fracture orthogonal monitoring wells were drilled with the same azimuth of S_{hmin}, (i.e., with a 356° trend), but at higher and lower plunges, forming a vertical "v" shape with the apex at the drift wall. The two fracture parallel monitoring wells were drilled orthogonal to the injection and production boreholes, forming a 12° tilled "v" shape with the apex at the drift wall. Corrected S_{hmin} directions from the kISMET borehole stress measurements are a 2˚ trend with a 9.3˚ plunge (Dobson et al., 2020).

The stages of EGS Collab Experiment 1 were analogous to those anticipated for commercial EGS reservoirs; stimulation to establish a hydraulic connection between the injection and production boreholes; and circulation to recover the thermal resource. This paper is concerned with the numerical simulation of the circulation stage of EGS Collab Experiment 1. A common discrete fracture network was developed following the stimulation stage that involved a hydraulic fracture emanating from the E1-I borehole at a stimulation notch located at 164 ft (50 m) from the borehole collar, and intersecting a natural fracture, termed the OT-P Connector, before crossing the E1-P borehole and intersecting the E1-PDT monitoring borehole (Neupane et al., 2019), as shown in Figure 1. Distributed temperature sensor data indicate intersection of the hydraulic fracture with E1-OT at 154.2 ft (47.0 m) from the borehole collar, and E1-PDT at 65.6 ft (20.0 m) and 49 ft (14.9 m). DTS additionally indicated a connection between a natural fracture, termed the PDT-OT connector, with the E1-PDT borehole at 131.2 ft (40 m) from the borehole collar. Extension of the hydraulic fracture in the direction opposite of the E1-P borehole was assumed to be minimal due to numerical simulations of the hydraulic fracture trajectory under the influence of a decreasing stress gradient toward the drift created by the drift cooling (Fu et al., 2018). Microseismic monitoring has validated this conclusion.

From perspective of numerically simulating the circulation stage of EGS Collab Experiment 1, the system comprises the rock matrix, a series of hydraulically connected fractures, and eight boreholes (two open and six grouted). The experiment is driven by the injection of chilled water (i.e., around 11˚C), via a packed interval in E1-I spanning the hydraulic fracture generated from the notch at 164 ft (50 m) from the collar. Water is then recovered in the drift, via two intervals in E1-P; a packed interval, termed E1-PI, spanning the contact of the OT-P Connector fracture with E1-P, and the interval below this packed interval, termed E1-PB, but also via other flow pathways, such as natural fractures or fractured zones intersecting the drift, and grouted boreholes. A principal objective for this experiment is to determine whether conservative and partitioning tracer experiments serve as analogs for forecasting thermal recovery, thus requiring the numerical simulation of fluid flow, heat transport, and tracer transport. A numerical simulation approach was sought that allowed for solutions on workstation class computers (i.e., multi-core shared-memory architectures), those that would be more practically available to commercial EGS operators. The use of an embedded fracture approach to model the coupled processes of fluid flow, geomechanics, and rock failure in the development of hydraulic networks for EGS via stimulation, including hydraulic fracturing and shear stimulation

(Norbeck et al., 2016), inspired the development of a numerical simulator comprising three discretized domains; matrix, embedded fractures, and embedded boreholes, solved fully coupled and simultaneously. Transfer terms allow the exchange of fluid, heat, solutes, and species between the three domains: fractures-rock matrix, boreholes-rock matrix, and fractures-boreholes, conserving component and tracer mass and energy.

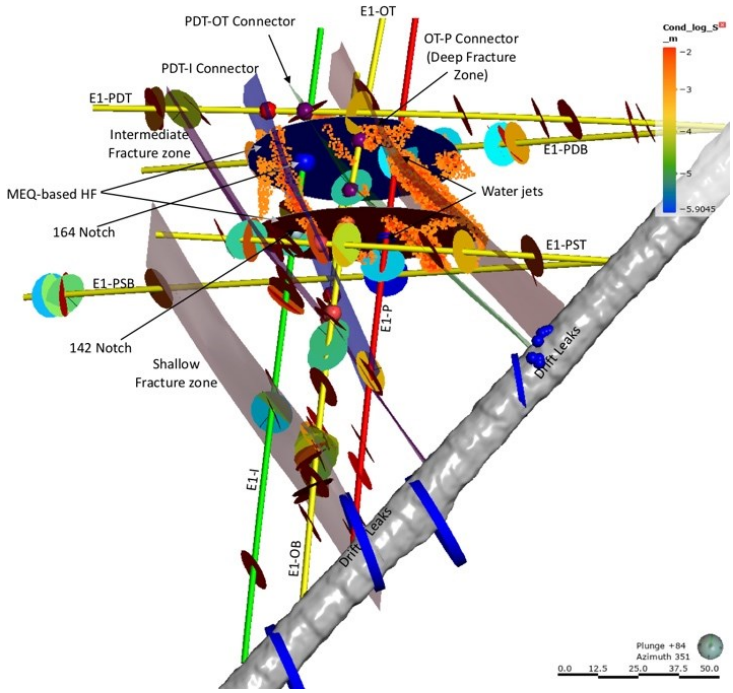

Figure 1: E1 testbed with E1-I borehole in green, E1-P borehole in red, monitoring boreholes in yellow, with 5 labeled natural fractures, and with purple spheres showing the location of DTS temperature anomalies during the hydraulic fracture stimulation at the 164' (50 m) notch

2. MATHEMATICAL MODEL

The three-domain numerical modeling framework was developed from the STOMP-GT (Subsurface Transport Over Multiple Phases – GeoThermal) numerical simulator, an operational mode of the STOMP suite of simulators (Oostrom et al., 2003; Oostrom and White, 2004; White and Oostrom, 2000), developed at the Pacific Northwest National Laboratory. STOMP-GT solves conservation equations for water mass, air mass, salt mass and energy, with capabilities for modeling coupled geochemical processes via its ECKEChem module and coupled porothermoelastic geomechanics via its finite-element based GeoMech module. This code was applied previously to determine the temperature environment within the EGS Collab Experiment 1 Testbed (Fu et al., 2018), but without the embedded fracture and borehole modeling capabilities. The STOMP-GT simulator solves governing conservation equations and associated constitutive equations for multifluid flow and transport via the finite-volume approach, with backward Euler time discretization, and Newton-Raphson iteration to resolve nonlinearities. The computational domain is based on hexahedra, yielding structured boundary fitted discretization of the rock matrix. For geochemical modeling an operator-split approach is used involving sequential transport and local reactions of equilibrium, conservation, and kinetic type reactions. Geomechanical displacements are solved at the eight nodes of the hexahedra using the finite-element method, with sequential iteration using the fixed-stress scheme (Kim et al., 2011) with coupled flow and transport. Embedded fractures and boreholes were incorporated into the simulator as additional finite-volume grid cells. Fractures boundaries are defined as polygons in three-dimensional space and then discretized into triangles, with finite aperture, creating a volume delineated by the planar triangle and aperture. Boreholes are defined by piece-wise trajectories and radii, following the well models developed for the STOMP-CO2 simulators (White et al., 2013). This three-domain approach yields a Jacobian matrix which is banded within the rock matrix equations with a seven-point stencil of 4x4 blocks (i.e., water mass, air mass, salt mass, and energy), banded within the fracture equations with a four-point stencil of 4x4 blocks, and banded within the borehole equations with a three-point stencil of 4x4 blocks. The inter-domain connections yield additional 4x4 blocks via the transfer terms between the three domains: fractures-rock matrix, boreholes-rock matrix, and fractures-boreholes, conserving component and tracer mass and energy.

The central concept for this mathematical modeling approach is that fractures and boreholes are embedded in the matrix grid structure, that is no attempt is made to alter the matrix grid structure with respect to the embedded fractures and boreholes. This assumption, therefore, allows for single fracture triangles to intersect multiple matrix grid cells and multiple fracture triangles to intersect single matrix grid cells. A search algorithm is used to define connections between fracture triangles and matrix grid cells; where, the first check involves identifying in which matrix grid cells the three fracture triangle vertices reside (White et al., 2013). Transfer functions for fluid flow, heat transport and solute and reactive species transport between fracture triangles and matrix grid cells, require surface areas and distances between the fracture triangle and matrix grid cells. Surface areas are computed based on the exposed surface area of the fracture triangle to the matrix grid cell, and separation distances are computed by dividing the matrix grid cell into 512 sub-blocks

(i.e., 8x8x8 sub-blocks) and computing the average distance between the fracture triangle centroid and the 512 sub-blocks. Aqueous and gas flow between fracture triangles and matrix grid cells is modeled as multifluid Darcy flow, with upwind weighting of fluid density, viscosity, and relative permeability and matrix intrinsic permeability defining the overall intrinsic permeability. Heat transport between the fracture triangle and matrix grid cell considers an advective heat transfer coefficient at the fracture surface, conduction across the matrix grid cell, and advective flux of enthalpy across the fracture triangle to matrix grid cell. The enthalpy of diffusing components across the interface is ignored. Solute and reactive species transport between the fracture triangle and matrix grid cell follows the scheme of Patankar (Patankar, 1980) to combine advection and diffusion. Intrinsic permeability with a fracture triangle is computed via the cubic law as a function of the local aperture.

Boreholes are specified via three-dimensional piece-wise trajectories through the rock matrix domain, with each piece of the trajectory being defined by a starting and ending coordinate location in the global coordinate framework. Borehole trajectories are discretized into borehole nodes; where, borehole nodes are defined as linear sub-sections of the borehole trajectory. Borehole nodes start and end at either the point at which the borehole trajectory intersects a matrix grid cell surface or at the starting or ending point of a borehole interval, as shown in Figure 2(a), in a two-dimensional domain. Fluid flow between a borehole node and rock matrix grid cell is modelled with a modified Peaceman well index formulation. The modification, known as the projection well index (Shu, 2005), involves the projection of the linear well interval segments onto the principal orthogonal axes of the computational grid. A Peaceman well index is then computed for each of the three orthogonal directions and the overall well index for the node is computed as the square root of the sum of the squares of the directional Peaceman well indices:

$$WI_x = \left[\frac{2\,\pi\sqrt{k_y\,k_z}\,L_x}{\ln\left(\frac{r_{o,x}}{r_{bh}}\right)+s_{bh,m}}\right];\; WI_y = \left[\frac{2\,\pi\sqrt{k_x\,k_z}\,L_y}{\ln\left(\frac{r_{o,y}}{r_{bh}}\right)+s_{bh,m}}\right];\; WI_z = \left[\frac{2\,\pi\sqrt{k_y\,k_x}\,L_z}{\ln\left(\frac{r_{o,z}}{r_{bh}}\right)+s_{bh,m}}\right] \tag{1}$$

$$r_{0,x} = \left[\frac{\left(\left\{\frac{k_y}{k_z}\right\}^{1/2}\Delta z^2+\left\{\frac{k_z}{k_y}\right\}^{1/2}\Delta y^2\right)^{1/2}}{\left(\left\{\frac{k_y}{k_z}\right\}^{1/4}+\left\{\frac{k_z}{k_y}\right\}^{1/4}\right)}\right];\; r_{0,y} = \left[\frac{\left(\left\{\frac{k_x}{k_z}\right\}^{1/2}\Delta z^2+\left\{\frac{k_z}{k_x}\right\}^{1/2}\Delta x^2\right)^{1/2}}{\left(\left\{\frac{k_x}{k_z}\right\}^{1/4}+\left\{\frac{k_z}{k_x}\right\}^{1/4}\right)}\right];\; r_{0,z} = \left[\frac{\left(\left\{\frac{k_x}{k_y}\right\}^{1/2}\Delta y^2+\left\{\frac{k_y}{k_x}\right\}^{1/2}\Delta x^2\right)^{1/2}}{\left(\left\{\frac{k_x}{k_y}\right\}^{1/4}+\left\{\frac{k_y}{k_x}\right\}^{1/4}\right)}\right] \tag{2}$$

$$WI = \sqrt{(WI_x)^2 + \left(WI_y\right)^2 + (WI_z)^2} \tag{3}$$

where, k_x, k_y, k_z, L_x, L_y, L_z, $r_{o,x}$, $r_{o,y}$, $r_{o,z}$, $s_{bh,m}$, WI_x, WI_y, WI_z, WI, Δx, Δy, and Δz are directional intrinsic permeability, directional component borehole node lengths (shown in Figure 2(b)), directional equivalent grid node radius, borehole-matrix skin factor, directional component Peaceman well index, composite Peaceman well index, and directional grid cell spacing, respectively. Heat transport between the borehole and matrix grid cell considers an advective heat transfer coefficient on the borehole wall, conduction across the matrix grid cell, and advective flux of enthalpy across the borehole node to matrix grid cell. Conduction heat transfer from the borehole surface to matrix grid cell is modeled in an analogous method to the Peaceman well index, with the directional thermal conductivity, replacing the intrinsic permeability in Eqns. (1) and (2), and eliminating the skin factor. Solute transport, and reactive species transport between the borehole node and matrix grid cell is analogous to that between fracture triangles and matrix grid cells.

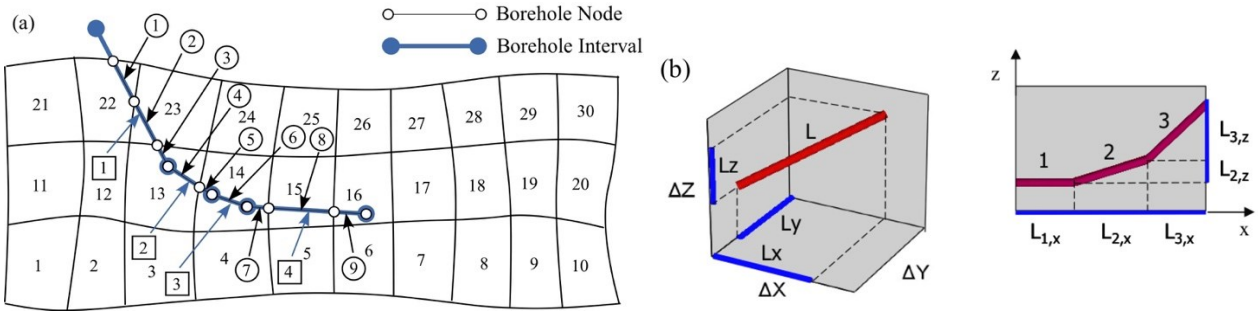

Figure 2: (a) Borehole interval and borehole node specification schemes, (b) borehole trajectory projected onto coordinate axes and borehole segments projected onto coordinate axes (image from Shu, 2005).

Transfer functions for fluid flow, heat transport, and solute and reactive species transport are additionally required for connections between borehole nodes and fracture triangles and intersections of fractures triangles from different fractures. Borehole to fracture connections are determined from a search algorithm identifying geometric intersections of a borehole node with a fracture triangle. For these connections fluid flow is modeled via a modified multifluid Darcy equation which includes a skin factor.

$$q_\ell = -\frac{k\,k_{r\ell}}{\mu_\ell\,(1+s_{bh,f})}\left[\nabla P_\ell + \rho_\ell\,g\,\vec{z}\right];\; q_g = -\frac{k\,k_{rg}}{\mu_g\,(1+s_{bh,f})}\left[\nabla P_g + \rho_g\,g\,\vec{z}\right] \tag{4}$$

where, q_ℓ, q_g, k, $k_{r\ell}$, k_{rg}, μ_ℓ, μ_g, $s_{bh,f}$, P_ℓ, P_g, ρ_ℓ, ρ_g, g, and $\vec{z}$ are the aqueous and gas flux, intrinsic permeability, aqueous and gas relative permeability, aqueous and gas viscosity, borehole to fracture skin factor, aqueous and gas pressure, aqueous and gas density, acceleration of gravity, and gravitational unit vector, respectively. The borehole to fracture skin factor is a convenient modeling approach for accounting for additional flow resistance between the borehole and entrance to the fracture, representing numerically flow resistances, such as near borehole tortuosity. Unlike some discrete fracture network modeling approaches, such as DFNWORKS (Hyman et al., 2015), where grids conform at fracture intersections, the modeling approach for this embedded fracture scheme allows for partial connections of fracture triangles between two fractures, as shown in Figure 3(a). Distances between fracture triangle centroids for fracture-fracture intersections are the cumulative distances from the triangle centroids to the midpoint of the triangle-triangle intersection length. Whereas, skin factor is generally associated with near wellbore permeability degradation or potentially enhancement in geologic reservoirs in porous media, the skin factor model of Eqn. (4), was adopted for modeling additional flow resistances at the intersection of two fracture triangles of different fractures, such as shown in Figure 3(b).

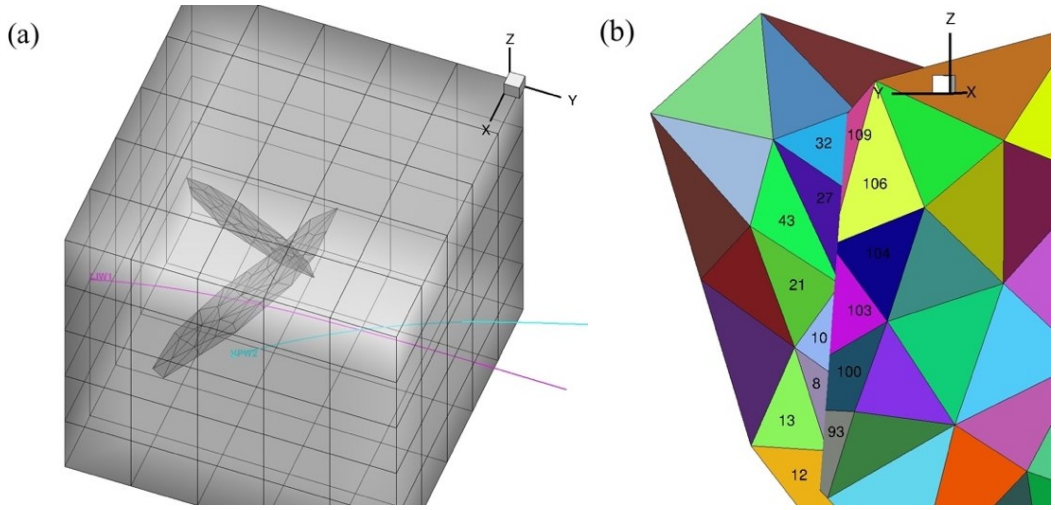

Figure 3: (a) 5 x 5 x 5 rock matrix domain with two embedded fractures and two embedded boreholes, (b) detail of fracture-fracture intersection, showing partial and multiple fracture triangle connections, such as fracture triangle 100 being partially connected to fracture triangles 8 and 10.

3. FRACTURE AND BOREHOLE NETWORK OF EGS COLLAB EXPERIMENT 1

The EGS Collab Experiment 1 (E1) testbed comprises eight HQ-diameter (i.e., 9.6 cm) continuously cored sub-horizontal boreholes, the rock volume surrounding those boreholes, a double-track portion of the 4850 Level West Access Drift (drift), stimulated hydraulic fractures, and existing natural fractures. Two of the boreholes were drilled in the direction of the minimum principal stress and designated to be the injection (E1-I) and production (E1-P) boreholes. Five notches were created within the lower one half of E1-I to serve as initiation points for the hydraulic fracture stimulations (Morris et al., 2018). The remaining six boreholes were instrumented with accelerometers, continuous active-source seismic monitoring (CASSM), electrical resistivity tomography (ERT) electrodes, passive hydrophones, distributed temperature sensors (DTS), distributed strain sensors (DSS), and thermistors and grouted with a mixture of ground blast furnace slag, ground pumice, and Portland cement. The E1-OT and E1-OB borehole were drilled orthogonal to the anticipated hydraulic fracture, and the E1-PST, E1-PSB, E1-PDT, and E1-PDB boreholes were drilled parallel to the anticipated hydraulic fracture, with E1-PST and E1-PSB being shallower, and E1-PDT and E1-PDB being deeper than the fracture initiation point along the depth of E1-I. The vertical boreholes drilled for the kISMET project (Oldenburg et al., 2016) near the E1 testbed suggested few natural fractures would be encountered within the testbed. Structural mapping of the drift (Roggenthen et al., 2018; Ulrich et al., 2018), several hydraulic fracturing experiments, and hydraulic flow testing activities (Neupane et al., 2019) revealed that the E1 testbed had cross-borehole hydraulic connectivity via natural fractures. These fractures and weep zones have a general NW-SE strike and steep dip (trend/plunge of the mean pole is 51°/2.5°) and are shown in Figure 4 as named features (i.e., Shallow Zone Fracture, Intermediate Zone Fracture, PDT-I Connector, PDT-OT Connector, and OT-P Connector (Deep Fracture Zone)).

A computational domain was developed to model the chilled water experiment, which started May 8, 2019 (10:15 MDT, 17:15 UTC) with the circulation of chilled water through the down-borehole heat exchanger within E1-I, cooling the temperature of the water injected into the hydraulic fracture at the 164' (50 m) notch, but also cooling the rock around E1-I. At this writing the chilled-water circulation test continues, after 266 days of nearly uninterrupted circulation. Outside of system outages, the chilled water injection rate was maintained at 400 ml/min. Throughout this experiment a straddle packer was located over the intersection of the OT-P Connector fracture and E1-P at a depth of 121.75 ft (37.1 m) from the borehole collar, allowing for the recovery of water from the region with the straddle packer interval (E1-PI) and below the interval (E1-PB), where the hydraulic fracture intersects the E1-P borehole. Water recovery was recorded during the chilled water experiment via flow meters from E1-PI, E1-PB, E1-PST, E1-PSB, E1-PDT, E1-PDB, E1-OT, E1-OB, E1-IB (below the injection straddle packer interval of E1-I), E1-IC (collar of E1-I), and manually from the weep zone (noted as the Shallow Fracture Zone) at the drift rib, using a water collection ledge carved into the drift rib on April 26, 2109. Water flows from all of the metered locations were noted throughout the course of the chilled water experiment, but near the end of the

experiment water production was predominately from E1-PB and E1-PI, with small amounts from E1-PST and E1-PDT. Volumetric recovery of the injected water approached 98% near the end of the experiment. For the first stage of the numerical simulation of the chilled water experiment, a computational domain was sought that was sufficiently complex to match the volumetric, thermal and tracer recoveries observed in the experiments, but as simple as possible.

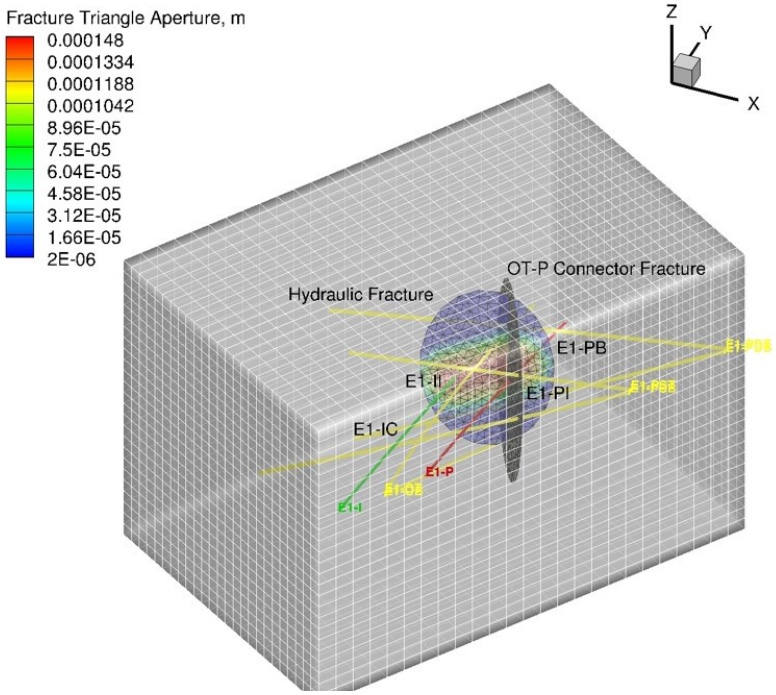

Figure 4: Computational grid showing structured rock matrix grid in white, hydraulic and natural fracture triangle grids in black, and location of the borehole nodes for intervals E1-II, E1-IC, E1-PB, and E1-PI.

This first-tier computational domain is shown in Figure 4 and involves a volume of rock, discretized with a structured mesh; the hydraulic and OT-P fractures, discretized as fracture triangles, and four sections of boreholes, discretized as borehole nodes (E1-II (injection interval), E1-IC (chilled loop interval), E1-PI (production interval), and E1-PB (below production interval)). The rock volume is aligned with the drift, rotated 33.5˚ to the east of the Homestake coordinates, shown in the upper right-hand corner of Figure 4, and extended 50 m orthogonal from the drift, 50 m vertically, and 75 m along the drift. The injection interval (E1-II) was discretized into 11 borehole nodes over a length of 1 m, intersecting the hydraulic fracture. The chilled loop interval was discretized into 130 borehole nodes from the collar to the top of the injection interval, and were assigned a fixed wall temperature of 11˚C. The production interval (E1-PI) was discretized into 11 borehole nodes over a length of 1 m, intersecting the OT-P Connector fracture, and the below production interval (E1-PB) was discretized into 11 borehole nodes over a length of 1 m, intersecting the hydraulic fracture. Dynamic fracture aperture is a planned future code capability, which will require a fracture opening model (e.g., boundary element model), so apertures across the hydraulic and OT-P Connector were assumed static. Hydraulic characterization tests indicated the OT-P Connector fracture to be highly permeable (Neupane et al., 2019), therefore, a uniform fracture aperture of 0.1 mm was assigned across the fracture of 15-m diameter. The aperture across the hydraulic fracture modeled the anticipated hydraulic fracture geometry determined from the fracture stimulation modeling under the thermally modified stress gradient (Fu et al., 2018). For this first-tier discretization, a modified Sneddon aperture distribution was generated along a path from the injection point to 2 m above the intersection of the hydraulic fracture with E1-PB, using a channel radius. Maximum aperture and channel radius of the hydraulic fracture were modeling parameters. Other modeling parameters were the *s* parameters at the intersections of E1-I and hydraulic fracture, E1-PI and OT-P Connector fracture, and E1-PB and hydraulic facture, and the aperture of the OT-P Connector fracture.

4. NUMERICAL SIMULATIONS OF EGS COLLAB EXPERIMENT 1

Thermal recovery and tracer recovery simulations were executed against the chilled water experiments in the E1 testbed. Thermal recovery simulations used the three-domain discretizations, starting with an initial temperature distribution determined from the drift cooling history modeling (White, Fu, Ghassemi, et al., 2018). Boundary surfaces were assigned to be in equilibrium with the initial temperature distribution and the pore water was assumed to be in hydrostatic equilibrium with pressure of 1 MPa at the bottom of the domain. Far-field pore pressure was not obtained during the experiments. Fluid in the fractures was initialized at 20˚C and in hydrostatic equilibrium with the pore pressure. The thermal recovery simulations were principally concerned with matching the observed injection pressures, volumetric recoveries and temperatures in the E1-PB and E1-PI intervals. Injection rates were maintained at 400 ml/min and fluid pressures in E1-PB and E1-PI were in hydrostatic equilibrium with a water surface open to atmospheric conditions at the E1-P collar in the drift. Tracer simulations were executed with shorter time steps to honor a Courant number limit of 0.5, starting from selected points in time during the thermal recovery simulations. Tracer recovery simulations were separate from the thermal recovery

simulations. Tracers were introduced into the E1-II interval as a pulse of tracer at a unit concentration. Petrophysical properties of the rock matrix (i.e., phyllite) used in the numerical simulation are listed in Table 1. Values for grain density, and grain specific heat were equivalent to those used by Ashworth in the numerical simulations (Ashworth, 1983) of the 8000 Level drift. Thermal conductivity and intrinsic permeability were determined from 1-dimensional simulations of drift cooling with evaporation, compared against the kISMET measurements of Roggenthen (Roggenthen and King, 2017). Ashworth (Ashworth, 1983) determined a thermal conductivity of 3.6 W/m K from laboratory measurements, lower than the value of 5.0 W/m K, used in this study. The capillary pressure versus saturation function was the van Genuchten model (van Genuchten, 1980) with a Webb extension (Webb, 2000), and the aqueous and gas relative permeabilities were computed from the Mualem model (Mualem, 1976).

Table 1. Experiment 1 Testbed Phyllite Petrophysical Properties

Property	Value	Property	Value	Property	Value
Grain Density	2900 kg/m^3	Intrinsic Permeability	1.0 x 10^{-19} m^2	van Genuchten m	0.346
Porosity	0.01	Thermal Conductivity	5.0 W/m K	Residual Saturation	0.06
Pore Compressibility	7.2 x 10^{-16} 1/Pa	van Genuchten α	0.186 1/m	Oven Dry Head	1.0 x 10^5 m
Grain Specific Heat	805 J/kg K	van Genuchten n	1.529		

4.1 Benchmark Observational Data

The chilled water experiment in E1 testbed started with the cooling of the injected water via a tube-in-tube heat exchanger on May 8, 2019 (10:15 MDT, 17:15 UTC) and has continued with sporadic shut-down periods to this writing. Key experimental data for these numerical simulations have been the injection flow rate, production flow rates, injection fluid temperature and production fluid temperatures in E1-PB and E1-PI. Temperatures in E1-I, E1-PB, and E1-PI were measured via unencapsulated thermistors, and those temperature measurements became suspect near the end of the chilled water experiment, at which point the thermistors were replaced with fully encapsulated versions. Inspection of the unencapsulated thermistors revealed water seepage into the insulation/jacket, and the temperature data for E1-PB and E1-PI throughout a majority of the experiment were discarded. Outside of the shut-down periods the injection flow rate, see Figure 5, was maintained at 0.4 L/min. The injection pressure, however, increased steadily over the course of the experiment with downward spikes occurring after shut-down periods and upward spikes generally occurring with injection temperature increases, as shown in Figure 6. Temperatures for E1-PB and E1-PI are shown as dashed lines in Figure 6, indicating the discarded data. The hydraulic fracture opening pressure was estimated during the stimulation to be 3190 psi (22 MPa). Early in the experiment flows from the E1-PST, E1-PDT, and the weep zone accounted for a large portion of the recovered flow, with fracture leakoff flow decreasing the percent of volumetric recovery. Late in the experiment flows from these monitoring boreholes and the weep zone declined, as did the leakoff. Near the end of the experiment volumetric recovery approached 96%, with 91.1% being recovered from E1-PB and E1-PI. Simulations reported below were executed against steady-flow conditions at the end of the experiment. The principal benchmark experimental observations from this time point are shown in Table 2. These benchmark observations were used in the determination of six unknown parameters: 1) s-factor at E1-I, 2) s-factor at E1-PB, 3) s-factor at E1-PI, 4) maximum aperture of the hydraulic fracture, 5) channel radius of the hydraulic fracture, and 6) aperture of the OT-P Connector fracture. The s-factors are shown in Eqn. (4), and represent additional flow resistance between the borehole and connecting fracture.

Table 2. Experiment 1 Benchmark Observations for the Thermal Recovery Simulations

Benchmark	Value	Benchmark	Value	Benchmark	Value	Benchmark	Value
Injection Flow Rate	0.400 L/min	E1-PB Flow Rate	0.130 L/min	E1-PI Flow Rate	0.226 L/min	Injection Temperature	12.46˚C
E1-PB Temperature	31.2˚C	E1-PI Temperature	29.7˚C	Injection Pressure	34.9 MPa	Fracture Opening Pressure	22.0 MPa
Peak Arrival Time for C-dots at E1-PB	67.32 min	Peak Arrival Time for C-dots at E1-PB	97.70 min				

4.2 Thermal Recovery Simulations

Thermal recovery simulations were initiated with the temperature field determined from the drift cooling history modeling (White, Fu, Ghassemi, et al., 2018), and hydrostatic conditions with pressure of 1 MPa at the bottom of the domain. Water in the hydraulic and OT-P Connector fractures were initialized at 20˚C. The upper, lower, and lateral boundary conditions were held constant, in equilibrium with the initial condition field. The outer surface of the E1-I borehole from the collar to the top of the packer string was maintained at

11˚C, as a no-flow boundary surface. The section of E1-I borehole within the packer interval was modeled as a string of borehole nodes with the upper node receiving water at 0.4 L/min at 11˚C. The sections of E1-P borehole beneath the packer interval (i.e., E1-PB) and within the packer interval (i.e., E1-PI) were modeled as strings of borehole nodes with the upper surface of the upper node maintained at 186.9 kPa and 181.7 kPa, respectively. These pressures were computed assuming hydrostatic conditions in E1-P, with the water level at the borehole collar. E1-I pressure records during the chilled water experiment (see Figure 5), showed three interesting features: 1) a gradual upward

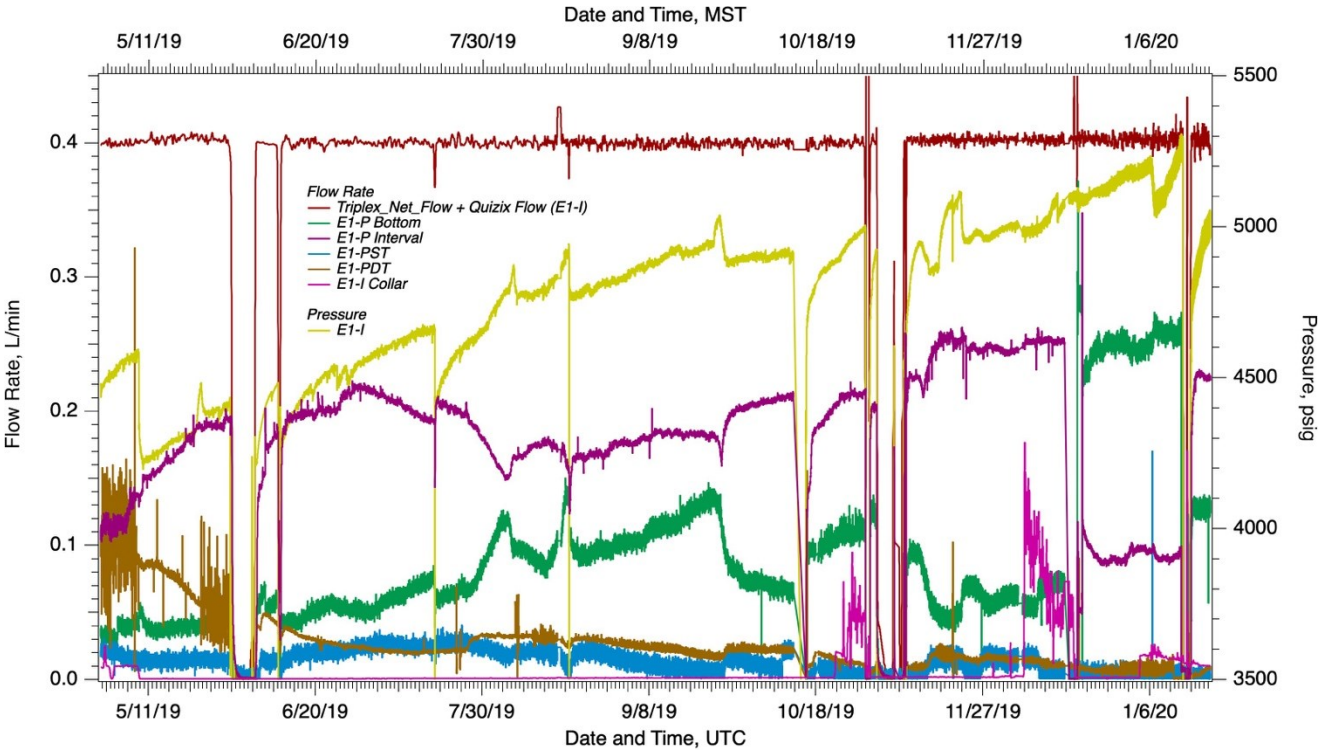

Figure 5: Flow rates and pressures during the chilled water experiment in E1 testbed.

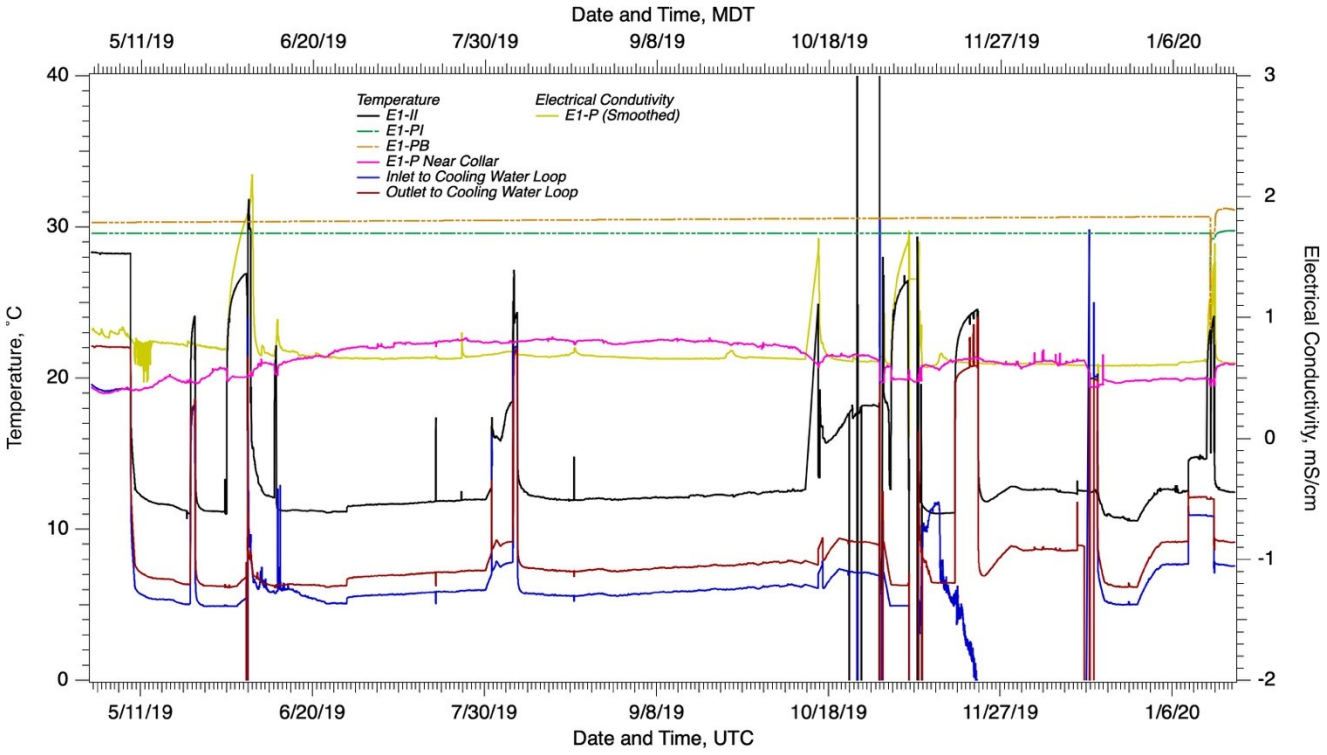

Figure 6: Temperature and electrical conductivity during the chilled water experiment in E1 testbed.

trend over time; 2) sharp reductions and recoveries after shut-down periods, and 3) rapid increases with increases in the temperature of the injection fluid. These features suggest a coupled thermal-geochemical-geomechanical mechanism controlling the flow resistance near the borehole. The simulations reported in this paper do not include a dynamic model of this flow resistance. Instead a single constant parameter (i.e., s-factor at E-PI) serves to define this flow resistance. During the hydraulic characterization of the E1 testbed, water jetting was noted in the E1-P borehole using a borehole camera with pressurization of the fracture network via water injection into E1-I (Dobson et al., 2020). These jets were noted at 127.8 ft (39.0 m) and 129.7 ft (39.5 m), near the projected intersection of the hydraulic fracture and E1-P. For the purposes of modeling, these jets were viewed as evidence of flow resistance between the fracture and borehole. As with E1-I, these flow resistances were modeled using constant parameters (i.e., s-factor at E1-PB and E1-PI). We recognized the potential for flow resistance to occur at the intersection of the hydraulic and OT-P Connector fractures but opted to assign an s-factor of zero for these intersections. The discovery of the OT-P Connector fracture during drilling suggested this fracture was transmissive, but other than the identification of the fracture in the E1-OT and E1-P cores, no hydraulic characterization data were available to parameterize this fracture. In the two-fracture network of these simulations the OT-P Connector fracture was modeled as having a uniform aperture of 0.1 mm across its entire 10-m diameter. The hydraulic fracture is discretized as a fracture with a 15-m diameter, but a Sneddon distribution of fracture aperture is assumed with a specified radius, around a channel centerline from the packer interval in E1-I to 2 m above the intersection with E1-P. This channel-centerline is modeled after the numerical simulations of the hydraulic fracture trajectory under the influence of a decreasing stress gradient toward the drift created by the drift cooling (Fu et al., 2018). The six modeling parameters were estimated using the PEST parameter estimation software (Doherty, 2016) against the observational benchmark data of Table 2, and the resulting values are shown in Table 3.

Table 3. Parameter values determined from PEST with STOMP-GT as the forward model.

Parameter	Value	Parameter	Value	Parameter	Value
$s_{bh,f}^{I}$	17.21	$s_{bh,f}^{PB}$	11.64	$s_{bh,f}^{PI}$	10.01
b_{max}	0.0220 mm	$r_{channel}$	5.51 m	b_{OT-P}	0.0926 mm

Simulation results for temperature versus time at E1-I, E1-PB, E1_PI, the hydraulic fracture near E1-I, the hydraulic fracture near E1-PB, and the OT-P Connector fracture near E1-PI are shown in Figure 7(a). The temperature point, shown in Figure 7(a), within E1-I is below the connection of E1-I and the hydraulic fracture, therefore, the temperature rises to a value above the injection temperature of 11˚C and then remains nearly constant. A jump in temperature occurs between E1-I and the hydraulic fracture near E1-I, as shown in Figure 7(a), due to the pressure drop of the flow resistance of s-factor at E1-I, via Joule-Thomson heating (Zhang et al., 2018). Flow across the hydraulic and OT-P Connector fractures results in heating of the water, with temperatures being slightly greater in hydraulic

fracture than the OT-P Connector at the intersection with E1-PI and E1-PB, respectively. This small temperature difference is due difference in flow paths for the two fractures and the radial thermal gradient surrounding the drift. Pressure drops from near-borehole flow resistances and modeled with the s-factors at E1-PB and E1-PI, yield small temperature increases of the fluid in the E1-P borehole, below and within the interval. Overall the temperature in E1-PB and E1-PI decrease slightly over the course of the experiment. Three dimensional views of the temperature profiles, an example of which is shown in Figures 8(a) and 8(b) at the end of the simulation, explain the reason for the slight temperature drop over time. After the initial transient, in which the injected chilled water reduces the temperature in the hydraulic fracture near E1-I, the changes in the temperature profile diminish, due to three factors: 1) the surface area of the fractures, 2) the low flow rate of 0.4 L/min through the fracture network, and the high rock thermal conductivity of 5.0 W/m K. These three factors yield scenario of very low thermal depletion of the rock matrix over the experimental period. The isotherm in Figure 8(a) shows the impact of the cooling along E1-I in the temperature profiles in E1-PSB and E1-PST, which showed locally depressed DST profiles from the initial radial distributions near the 30-m depth.

Volumetric flow rates in the experiment vary over time, with the monitoring boreholes and weep zones contributing to the recovered volumes. These simulations did not include those production pathways, but their inclusion is a matter of adding these boreholes as embedded features and adjusting the permeability of the borehole fill to create matches in the production volumes. Injection flow rates are specified as simulation inputs, but flow rates into E1-PB and E1-PI, and the leakoff flow rates are simulation outcomes. Flow rates into E1-P are controlled through the specified fixed pressures (i.e., the hydrostatic pressures for a water level at the borehole collar) and the s-factors for each production interval (i.e., E1-PB and E1-PI), as shown in Figure 7(b). The initial pore pressure was not measured during the experiment, so an estimate of the far-field pressure was made for these simulations at 1.0 MPa. This value places the pore pressure within the injection pressure of 34.9 MPa and the production pressure of 0.18 MPa. This makes a portion the fractures exposed to initial pore pressures above and below the fracture pressures during flow, yielding positive leakoff near the injection borehole and negative leakoff near the production borehole. The net effect for these simulations was a slightly negative integrated leakoff for the system, as shown in Figure 7(b).

4.3 Tracer Recovery Simulations

Over the course of the chilled-water circulation test a total of ten tracer experiments have been conducted in E1 testbed (Neupane et al., 2020). Non-DNA tracers injected into the fracture network are summarized in Table 3. Fluorescein tracers were injected and recovered during the hydraulic characterization tests prior to the chilled water injection test, but not during the test proper. At this writing tracer recoveries were available for the tracer experiments prior to those executed in late January 2020, for those tracers detectible in the drift via fluorescence (i.e., C-Dots, Rhodamine-B, and Phenol Acetate). Whereas both conservative (i.e., non-sorbing) and sorbing tracers were tested during the chilled water injection experiment, at the time of this writing, no data are available for the sorption coefficient with the E1 testbed phyllite rock. Batch experiments with crushed phyllite rock to determine sorption isotherms for Rhodamine-B will be conducted in late January 2020. Tracer simulations were executed under the flow conditions at the end of the thermal recovery simulations. Time stepping was limited by the flow and heat transport convergence time-stepping, but also by a Courant number limit of 0.5, globally applied over all three computational domains (i.e., rock matrix grid cells, fracture triangles, and borehole nodes). Sub-time stepping was used for the tracer transport calculations to honor the Courant limit. Tracers were introduced into the E1-I borehole as a slug at a concentration of 1.0 mol/ml for a period of 5.0 min. No accounting of the additional water injection associated with the tracer injection of the field experiment was included. Tracer concentrations were then tracked at selected points in the computational domain, along with integrated amounts of tracer mass in all three domains. Tracer concentration histories are shown in Figure 9(a) at selected locations within the fractures and boreholes. The tracer concentration peak was higher and arrived earlier (i.e., peak arrival at 23.05 min) in E1-PB, versus E1-PI (i.e., peak arrival at 37.55 min). Phenol acetate recoveries from the tracer experiment on 10/22/19 showed earlier peak arrivals in E1-PB versus E1-PI, but the peak arrival times were significantly delayed from the simulation results, 103.2 min and 124.2 min, respectively for E1-PB and E1-PI. This would suggest the flow path is more tortuous than that used in the simulations. The normalized distribution of tracer between the three domains over time is shown in Figure 9(b), which shows a portion of the tracer remains distributed in the fracture domain after peak arrivals at both intervals in E1-P. Only small amounts of tracer migrate into the matrix, due to the small matrix permeability and short residence time in the fracture.

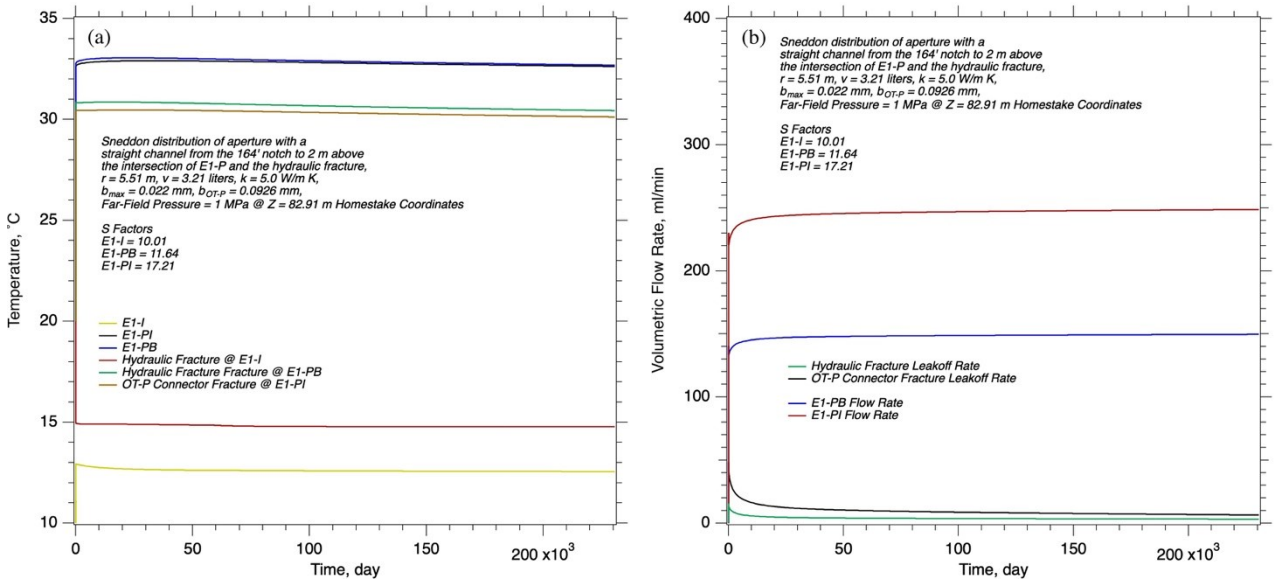

Figure 7: (a) Temperature histories for initial PEST simulations, (b) volumetric flow rate histories for initial PEST simulations.

Table 3. Tracer characteristics and experiments

Tracer	Type	Notes	Dates
Chloride, Bromide	conservative soluble	laboratory analysis required	all
C-Dots	conservative non-soluble	3-5 nm diameter carbon core particle coated with a fluorescent polymer coating, detectable to 10 ppb	04/25/19, 05/01/19, 07/24/19, 10/22/19, 01/28/20
Rhodamine-B	sorbing soluble	detectible in the drift via fluorescence	04/29/19, 11/19/19, 01/29/20
Phenol Acetate	thermally reactive soluble	thermally reactive tracer in which the phenol acetate reacts with hydroxide to produce phenol and acetate	05/07/19, 05/09/19, 05/21/19, 07/24/19, 10/22/19

5. CONCLUSIONS

A central thrust of the EGS Collab project, funded by the United States Department of Energy, Geothermal Technologies Office (GTO) is to compare numerical simulation results against experiment observations at the meso-scale under *in-situ* stress conditions, leading to increased confidence in applying these analytical tools or identification of needed model developments for future applications at the Frontier Observatory for Research in Geothermal Energy (FORGE) or commercial EGS reservoirs. This numerical study was focused on modeling fluid flow, heat transfer, and tracer transport during a chilled water circulation test with the Experiment 1 testbed from early May 2019 through late January 2020. The fracture network through which the circulation test occurred had been previously established via a stimulation and hydraulic characterization campaign, and the injection pressures during the chilled water circulation test were limited to avoid extending the fractures in the network. Acoustic emission monitoring was used to detect changes in the fracture network during the experiment. An embedded fracture and modeling approach was applied in this study, built on three separate discretizations, a structured

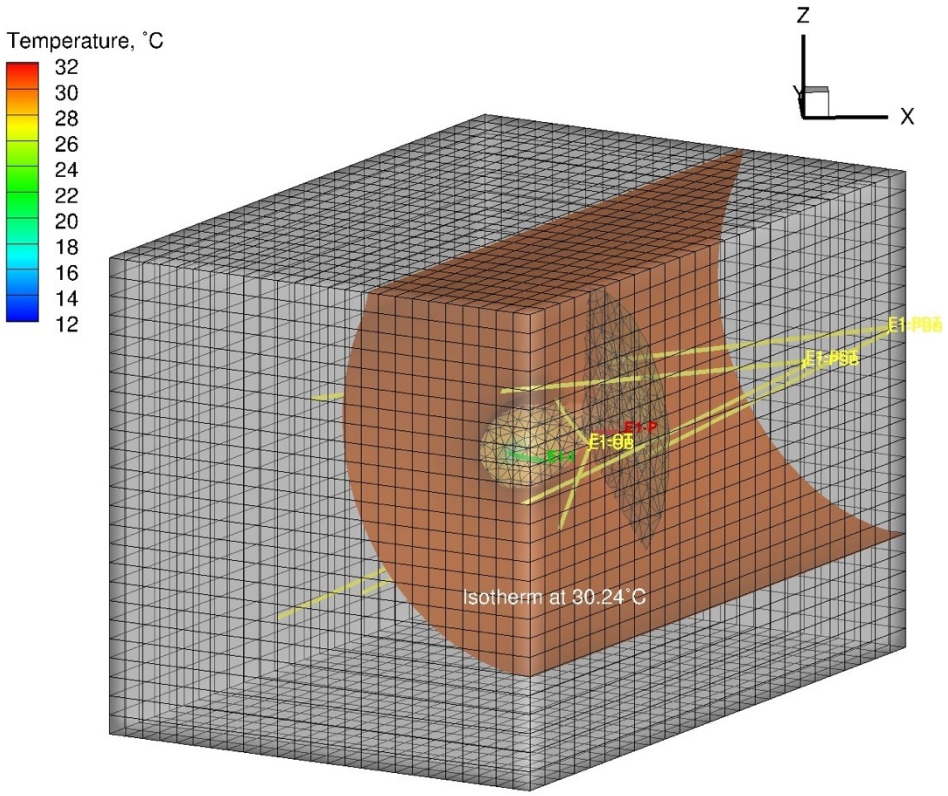

Figure 8: (a) Temperature profiles in the fracture and rock matrix at the end of the simulation (looking north.

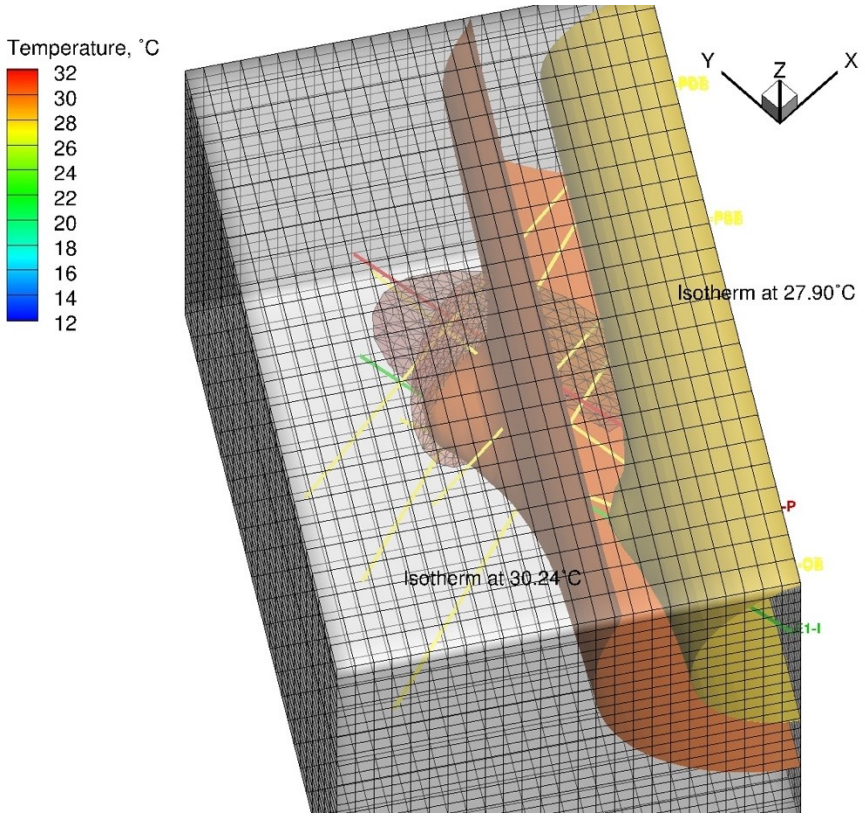

Figure 8: (b) deformations of the temperature isotherms in the rock matrix from the cooling along E1-I by the circulating chilling water (looking down toward the northeast).

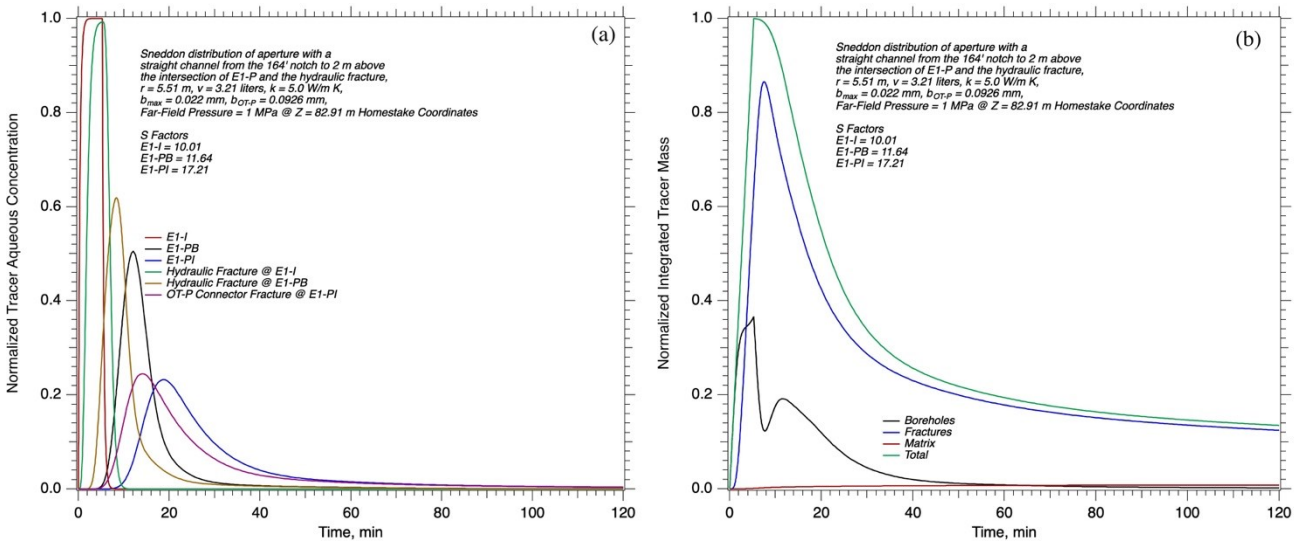

Figure 9: (a) Conservative tracer concentrations at E1-I, E1-PB, E1-PI, hydraulic fracture near E1-I, hydraulic fracture near E1-PB, and OT-P Connector fracture near E1-PI (b) normalized integrated tracer mass within boreholes, fractures, matrix and total.

hexahedron grid cell for the rock matrix, a planar triangular discretization with fixed aperture for the fractures, and a cylindrical discretization for the boreholes. Transfer functions were developed to compute fluid flow, heat transfer and tracer transport across the different domains. This numerical approach was adopted to keep computational efforts at the level of a workstation computer (i.e., multi-core, shared memory computer).

Flow resistance factors applied to the borehole-fracture connections allowed for calibration of the thermal recovery simulation against the experimental observations, assuming a fixed channel radius. This calibrated flow system, however, yield arrival times for the conservative tracers that were earlier than those observed in the experiments. New tracer experiments, under the current flow configuration in the E1 testbed, are scheduled, which will include both conservative and sorbing tracers. Tracer recovery results will then be used to estimate a flow channel radius. The numerical simulations and experimental observations do concur with respect to the contrast in responses between the thermal recovery and tracer recovery. Both the numerical simulation and the experimental observations show rapid recovery times for the tracers, yet negligible thermal breakthrough. The E1 testbed presented modelling challenges that were somewhat unique, in terms of parameterization. At first inspection it would seem that application of s-factors at E1-PB and E1-PI would be sufficient to create a pressure drop to near atmospheric conditions within the borehole, while maintaining the fracture pressures sufficiently elevated for flow. This sharp pressure drop at E1-PB and E1-PI, however, results in an increase in the production temperatures of several degrees from Joule-Thomson heating, eliminating the potential for agreement in simulated and observed production temperatures. S-factors applied at E1-I also result in a pressure drop and fluid heating, but that increase in temperature decays as the fluid moves across the fracture, allowing for an agreement in simulated and observed production temperatures. S-factors at E1-I, however, yield pressure drops that fail to maintain fracture pressures sufficiently elevated for flow. The embedded fracture and borehole modeling approach allowed for combined thermal and tracer recovery using the same computational framework and would additionally allow for geochemical modeling. In this first application of this newly implemented approach, fracture aperture and flow resistance factors were fixed. Future implementations of this modeling approach will consider modeling these parameters as being dynamic and dependent on temperature and effective stress. The relatively simple two-fracture model developed for this numerical study was able to capture the general responses of the flow network, thermal recovery and tracer recovery.

ACKNOWLEDGEMENTS

This material was based upon work supported by the U.S. Department of Energy, Office of Energy Efficiency and Renewable Energy (EERE), Office of Technology Development, Geothermal Technologies Office, under Award Number DE-AC52-07NA27344 with LLNL, Award Number DE-AC05-76RL01830 with PNNL, and Award Number DE-AC02-05CH11231 with LBNL. The United States Government retains, and the publisher, by accepting the article for publication, acknowledges that the United States Government retains a non-exclusive, paid-up, irrevocable, world-wide license to publish or reproduce the published form of this manuscript, or allow others to do so, for United States Government purposes. We thank the drillers of Agapito Associates, Inc., for their skill and dedicated efforts to create our test bed boreholes. The research supporting this work took place in whole or in part at the Sanford Underground Research Facility in Lead, South Dakota. The assistance of the Sanford Underground Research Facility and its personnel in providing physical access and general logistical and technical support is gratefully acknowledged.

REFERENCES

Ashworth, E., 1983. The applications of finite element analysis to thermal conductivity measurements. South Dakota School of Mines and Technology, Rapid City, SD, USA.

Dobson, P.F., Kneafsey, T., Blankenship, D., Valladao, C.A., Morris, J.P., Knox, H., Schwering, P., White, M.D., Doe, T., Roggenthen, W., Mattson, E., Podgorney, R., Johnson, T.C., Ajo-Franklin, J., Team, E.C., 2017. An Introduction to the EGS Collab Project. Geothermal Resources Council Transactions 41, 837-849.

Dobson, P.F., Kneafsey, T.J., Blankenship, D., Morris, J.P., Fu, P., Knox, H., Schwering, P., Ingraham, M., White, M.D., Johnson, T., Burghardt, J.A., Doe, T., Roggenthen, W., Neupane, G., Podgorney, R., Horne, R.N., Hawkins, A., Singh, A., Huang, L., Frash, L.P., Weers, J., Ajo-Franklin, J., Schoenball, M., Ulrich, C., Mattson, E., Uzunlar, N., Valladao, C.A., Team, E.C., 2020. The EGS Collab Project – Fracture Stimulation and Flow Experiments for Coupled Process Model Validation at the Sanford Underground Research Facility (SURF), South Dakota, USA, World Geothermal Congress 2020, Reykjavik, Iceland.

Doherty, J., 2016. PEST Model-Independent Parameter Estimation, User Manual Part I: PEST, SENSAN and Global Optimizers, 6th ed. Watermark Numerial Computing.

Duchane, D.V., Winchester, W.W., 1992. Hot Dry Rock Energy Annual Report Fiscal Year 1992. Los Alamos National Laboratory, Los Alamos, NM, USA.

Fu, P., White, M.D., Morris, J.P., Kneafsey, T.J., Team, E.C., 2018. Predicting Hydraulic Fracture Trajectory Under the Influence of a Mine Drift in EGS Collab Experiment I, 43rd Workshop on Geothermal Reservoir Engineering, Stanford University, Stanford, CA, USA.

Hyman, J.D., Karra, S., Makedonska, N., Gable, C.W., Painter, S.L., Viswanathan, H.S., 2015. DFNWORKS: A discrete fracture network framework for modeling subsurface flow and transport. Computers & Geosciences 84, 10-19.

Kim, J., Tchelepi, H.A., Juanes, R., 2011. Stability and convergence of sequential methods for coupled flow and geomechanics: Drained and undrained splits. Computer Methods in Applied Mechanics and Engineering 200, 2094-2116.

Kneafsey, T., Blankenship, D., Dobson, P.F., Knox, H., Johnson, T.C., Ajo-Franklin, J., Schwering, P., Morris, J.P., White, M.D., Podgorney, R., Roggenthen, W., Doe, T., Mattson, E., Valladao, C.A., Team, E.C., 2018. EGS Collab Project Experiment 1 Overview and Progress. Geothermal Resources Council Transactions 42.

Kneafsey, T., Blankenship, D., Dobson, P.F., Morris, J.P., White, M.D., Knox, H., Johnson, T.C., Ajo-Franklin, J., Schwering, P., Fu, P., Podgorney, R., Huang, L., Johnston, B., Roggenthen, W., Doe, T., Mattson, E., Valladao, C.A., 2019. EGS Collab Project: Accomplishments and Plans. Geothermal Resources Council Transactions 43, 366-367.

Morris, J.P., Dobson, P.F., Knox, H., Ajo-Franklin, J., White, M.D., Fu, P., Burghardt, J.A., Kneafsey, T., Blankenship, D., Team, E.C., 2018. Experimental design for hydrofracturing and fluid flow at the DOE Collab testbed, 43rd Workshop on Geothermal Reservoir Engineering. Stanford University, Stanford University, Stanford, CA, USA.

Mualem, Y., 1976. New Model for Predicting Hydraulic Conductivity of Unsaturated Porous-Media. Water Resources Research 12, 513-522.

Neupane, G., Mattson, E.D., Plummer, M.A., Podgorney, R., Team, E.C., 2020. Results of Multiple Tracer Injections Into Fractures in the EGS Collab Testbed-1, 45th Workshop on Geothermal Reservoir Engineering, Stanford University, Stanford, CA, USA.

Neupane, G., Podgorney, R., Huang, H., Mattson, E., Kneafsey, T., Dobson, P.F., Schoenball, M., Ajo-Franklin, J., Schwering, P., Knox, H., Blankenship, D., Johnson, T., Strickland, C.E., Team, E.C., 2019. EGS Collab Earth Modeling: Integrated 3D Model of the Testbed. Geothermal Resources Council Transactions 43, 380-401.

Norbeck, J.H., McClure, M.W., Lo, J.W., Horne, R.N., 2016. An embedded fracture modeling framework for simulation of hydraulic fracturing and shear stimulation. Computational Geosciences 20, 1-18.

Oldenburg, C.M., Dobson, P.F., Wu, Y., Cook, P.J., Kneafsey, T., Nakagawa, S., Ulrich, C., Siler, D.L., Guglielmi, Y., Ajo-Franklin, J., Rutqvist, J., Daley, T.M., Birkholzer, J.T., Wang, H.F., Lord, N.E., Haimson, B.C., Stone, H.L., Vigilante, P., Roggenthen, W.M., Doe, T.W., Lee, M.Y., Ingraham, M., Huang, H., Mattson, E.D., Zhou, J., Johnson, T.J., Zoback, M.D., Morris, J.P., White, J.A., Johnson, P.A., Coblentz, D.D., Heise, J., 2016. Intermediate-Scale Hydraulic Fracturing in a Deep Mine, kISMET Project Summary 2016. Lawrence Berkeley National Laboratory, Berkeley, CA, USA.

Oostrom, M., Meck, D.H., White, M.D., 2003. STOMP Subsurface Transport Over Multiple Phases, An Introductory Short Course. Pacific Northwest National Laboratory, Richland, WA, USA.

Oostrom, M., White, M.D., 2004. STOMP Subsurface Transport Over Multiple Phases Version 3.1 User's Guide. Pacific Northwest National Laboratory, Richland, WA, USA.

Patankar, S.V., 1980. Numerical Heat Transfer and Fluid Flow. Hemisphere, New York, NY, USA.

Roggenthen, W.M., Doe, T.W., Team, E.C., 2018. Natural Fractures and Their Relationship to the EGS Collab Project in the Underground of the Sanford Underground Research Facility (SURF), 52nd U.S. Rock Mechanics/Geomechanics Symposium. American Rock Mechanics Association, pp. 1190-1199.

Roggenthen, W.M., King, D.K., 2017. Quick Review of T data for kISMET Area. Lawrence Berkeley National Laboratory, Berkeley, CA, USA.

Shu, J., 2005. Comparison of Various Techniques for Computing Well Index. Stanford University, Stanford, CA, USA.

Ulrich, C., Dobson, P.F., Kneafsey, T.J., Roggenthen, W.M., Uzunlar, N., Doe, T.W., Neupane, G., Podgorney, R., Schwering, P., Frash, L.P., Singh, A., 2018. The distribution, orientation, and characteristics of natural fractures for Experiment 1 of the EGS Collab Project, Sanford Underground Research Facility, 52nd U.S. Rock Mechanics/Geomechanics Symposium. American Rock Mechanics Association, pp. 1252-1259.

van Genuchten, M.T., 1980. A closed-form equation for predicting the hydraulic conductivity of unsaturated soils. Soil Science Society of America Journal 44, 892-898, https://www.doi.org/810.2136/sssaj1980.03615995004400050002x.

Webb, S.W., 2000. A simple extension of two-phase characteristic curves to include the dry region. Water Resources Research 36, 1425-1430.

White, M.D., Bacon, D.H., White, S.K., Zhang, Z.F., 2013. Fully Coupled Well Models for Fluid Injection and Production. Energy Procedia 37, 3960-3970.

White, M.D., Fu, P., Ghassemi, A., Huang, H., Rutqvist, J., Johnston, B., Team, E.C., 2018. Numerical Simulation Applications in the Design of EGS Collab Experiment 1, 43rd Workshop on Geothermal Reservoir Engineering, Stanford University, Stanford, CA, USA.

White, M.D., Fu, P., Huang, H., Rutqvist, J., Johnston, B., Team, E.C., 2018. Predictive Modeling of Fracture Generation and Fluid Circulation and Comparisons to Observations for a Meso-Scale Enhanced Geothermal System Experiment – EGS Collab Project, Computational Methods in Water Resources XXII, Saint-Malo, France.

White, M.D., Fu, P., McClure, M.W., Danko, G., Elsworth, D., Sonnenthal, E., Kelkar, S., Podgorney, R., 2018. A suite of benchmark and challenge problems for enhanced geothermal systems. Geomechanics and Geophysics for Geo-Energy and Geo-Resources 4, 79-117.

White, M.D., Johnson, T.C., Kneafsey, T., Blankenship, D., Fu, P., Wu, H., Ghassemi, A., Lu, J., Huang, H., Neupane, G., Oldenburg, C.M., Doughty, C.A., Johnston, B., Winterfeld, P., Pollyea, R., Jayne, R., Hawkins, A., Zhang, Y., Team, E.C., 2019. The Necessity for Iteration in the Application of Numerical Simulation to EGS: Examples from the EGS Collab Test Bed 1, 44th Workshop on Geothermal Reservoir Engineering, Stanford University, Stanford, CA, USA.

White, M.D., McClure, M.W., Fu, P., Cheng, Q., Elsworth, D., Gan, Q., Hao, Y., Im, K.J., Safari, R., Tao, Q., Xia, Y., Podgorney, R., Danko, G., Bahrami, D., Chiu, K., Fang, Y., Gao, Q., Horne, R.N., Norbeck, J., Sesetty, V., White, S.K., Kelkar, S., Ghassemi, A., Barbier, C., Detourney, C., Furtney, J.K., Guo, B., Huang, H., Rutqvist, J., Sonnenthal, E., Wong, Z., 2016a. Benchmark Problems of the Geothermal Technologies Office Code Comparison Study. Pacific Northwest National Laboratory, Richland, WA, USA.

White, M.D., McClure, M.W., Fu, P., Cheng, Q., Elsworth, D., Gan, Q., Hao, Y., Im, K.J., Safari, R., Tao, Q., Xia, Y., Podgorney, R., Danko, G., Bahrami, D., Chiu, K., Fang, Y., Gao, Q., Horne, R.N., Norbeck, J., Sesetty, V., White, S.K., Kelkar, S., Ghassemi, A., Barbier, C., Detourney, C., Furtney, J.K., Guo, B., Huang, H., Rutqvist, J., Sonnenthal, E., Wong, Z., 2016b. Challenge Problems of the Geothermal Technologies Office Code Comparison Study. Pacific Northwest National Laboratory, Richland, WA, USA.

White, M.D., Oostrom, M., 2000. STOMP Subsurface Transport Over Multiple Phases, Version 2.0, Theory Guide. Pacific Northwest National Laboratory, Richland, WA, USA.

Zhang, Y., Doughty, C.A., Pan, L., Kneafsey, T., 2018. What Could We See at The Production Well Before The Thermal Breakthrough?, 43rd Workshop on Geothermal Reservoir Engineering, Stanford University, Stanford, CA, USA.

Zyvoloski, A.G., 2007. FEHM: A control volume finite element code for simulating subsurface multi-phase multi-fluid heat and mass transfer. Los Alamos National Laboratory, Los Alamos, NM, USA.